



## Research Paper

## Modelling of liquid oxygen and nitrogen injection under flashing conditions

T. Lyras<sup>\*</sup>, I.K. Karathanassis, N. Kyriazis, P. Koukouvinis, M. Gavaises

School of Science &amp; Technology, City, University of London, Northampton Square, EC1V 0HB, London, UK



## ARTICLE INFO

## Keywords:

Cryogenic fluids  
LOx  
LN<sub>2</sub>  
Rocket engine  
Real-fluid thermodynamics  
Flash boiling  
Compressible flow

## ABSTRACT

The present numerical investigation of two-phase flashing flows examines the injection of liquid oxygen and liquid nitrogen into near-vacuum conditions prevailing in the upper-stage boosters of rocket engines. The predictive capability of a pressure-based solver and a density-based solver, each employing distinct approaches related to the imposed phase-change rate and thermodynamics closure, has been comparatively evaluated. Regarding the pressure-based solver, the departure from thermodynamic equilibrium during phase-change has been taken into account via the implementation of a bubble-dynamics model employing the Hertz-Knudsen equation. In contrast, the density-based solver relies on the adoption of thermodynamic equilibrium while real-fluid thermodynamic properties are assumed by loading tabulated values to the solver. Each thermodynamic property value was calculated in advance by solving the Helmholtz Equation of State (EoS) for a wide range of density and internal energy conditions. Numerical findings have been compared against experimental data available in the literature. The comparison demonstrates the capability of both methodologies in capturing the evolution of cryogenic flashing flow expansion, phase-change, and spray formation. The salient features identified in the numerical results, i.e., the expansion sphere immediately downstream of the injector exit, the bell-shaped topology of the spray, as well as the dependency of the spray cone angle on superheat, are in agreement with experimental measurements. Especially the density-based approach has been proven highly accurate with respect to the steady expanding flow described by a level of superheat in the range of 3 to 245, while also being independent of any parameter tuning.

## 1. Introduction

Cryogenic propellants in liquid-state have been utilized since the 1960s [1] and are currently the selected type of propellants for many modern upper-stage rocket engines. The combination of LOx and LH<sub>2</sub> has been used to propel the main engines of NASA's space shuttle [2], Ares-I vehicle [3], the Centaur engine of Atlas rocket [4] and ESA's Ariane 5 upper stage engines [5], while SpaceX's Falcon and Blue Origin's BE-4 rocket, use as propellants a mixture of LOx/LCH<sub>4</sub> and LOx/Liquefied natural gas (LNG), respectively [6,7]. For the lower-stage engines, LOx/RP-1 is a very common propellant mixture with Saturn V, Atlas V, the Russian Soyuz and Falcon being some of the rockets that operate on it [8,9].

While the initial lift-off of a space launch vehicle takes place in atmospheric conditions, the upper-stage engines are expected to ignite and operate in near-vacuum conditions. Those low-pressure operating conditions of second-stage engines can lead to flash evaporation or flash boiling of the propellants during start-up, which can affect the ignition

process [10–13]. Investigation of cryogenic flash boiling is, therefore, essential for understanding and controlling the process. Extremely low pressure and temperature storage conditions required for cryogenic fluids, as well as the intense phase-change rates during flash evaporation, are hindering factors to the realization of experimental campaigns and, thus, the open literature relevant to the topic is relatively limited.

An early NASA report by Hendricks et al. [14] offers experimental data in terms of mass flow rates and pressure distribution of two-phase mixtures of LOx and LN<sub>2</sub> flowing through different types of converging–diverging nozzles for a wide range of sub- and super-critical conditions. Mayer and co-workers [15,16] presented flow visualizations and measurements related to the propellant injection (LOx/H<sub>2</sub>), mixing, evaporation, and combustion in a liquid rocket engine combustor at sub- and supercritical chamber pressures. The injection visualizations and studies under combusting conditions revealed a remarkable difference between subcritical spray formation and evaporation, and the supercritical injection and mixing processes. The experimental studies conducted on ONERA's Mascotte test bench [17,18] focus mainly on the combustion processes involved in cryogenic

<sup>\*</sup> Corresponding author.

E-mail address: [Theodoros.Lyras.2@city.ac.uk](mailto:Theodoros.Lyras.2@city.ac.uk) (T. Lyras).

Nomenclature		u	velocity (m s <sup>-1</sup> )
A	area (m <sup>2</sup> )	<i>Greek Letters</i>	
a	molar Helmholtz energy (J)	$\alpha$	volume fraction (-)
$\alpha^0$	dimensionless ideal gas contribution to the Helmholtz energy (-)	$\delta$	dimensionless density (-)
$\alpha^f$	dimensionless residual Helmholtz energy (-)	$\lambda$	accommodation coefficient (-)
c	speed of sound (m s <sup>-1</sup> )	$\lambda_g$	Taylor length scale (m)
d	diameter (m)	$\mu$	viscosity (N s m <sup>-2</sup> )
e	internal energy (J kg <sup>-1</sup> )	$\rho$	density (kg m <sup>-3</sup> )
k	thermal conductivity (W m <sup>-1</sup> K <sup>-1</sup> )	$\tau$	dimensionless temperature (-)
M	Mach number (-), $M = u/c$	<i>Subscripts</i>	
N	Finite element nodal shape function	c	critical
$\dot{m}$	mass flow rate (kg s <sup>-1</sup> )	exp	experimental value
n	nucleation site density	g	gas
L	length (m)	in	inlet
p	pressure (Pa)	int	interface
R	specific gas constant (J kg <sup>-1</sup> K <sup>-1</sup> )	max	maximum
Re	Reynolds number (-)	min	minimum
$R_g$	ideal gas constant, $R_g = 8.31446$ (J mol <sup>-1</sup> K <sup>-1</sup> )	n	node number
$R_p$	superheat (-), $R_p = p_{\text{sat}}(T_{\text{in}}) / p_{\text{out}}$	out	outlet
$\dot{R}$	phase-change rate kg m <sup>-3</sup> s <sup>-1</sup>	sat	saturation
T	temperature (K)	t	throat
t	time (s)	v	vapour

propellant LOx/H<sub>2</sub> systems, although the characteristics of LOx sprays have also been investigated. The work of Chehroudi et al. [19] is focused on LOx and LN<sub>2</sub> injection into environments composed of N<sub>2</sub>, He, Ar, and CO/N<sub>2</sub> mixtures. Boundary conditions vary from sub- to supercritical and the resulting flows were captured by a CCD camera with the use of backlit illumination. A Subsequent work by Chehroudi gives an overview of experimental efforts to elucidate the distinct features of high-pressure supercritical injection [20].

In contrast to the aforementioned publications that study the behaviour of cryogenic fluids for pressure regimes higher than atmospheric, experimental data on cryogenic flashing sprays at near-vacuum conditions are rare. A noteworthy mention should be made of the cryogenic facility at the Technical University of Munich (TUM) and the DLR facility, dedicated to fundamental research on cryogenic spray atomisation, ignition and combustion [21]. At TUM, Luo and Haidn [13] investigated a flashing LN<sub>2</sub> spray in a low-pressure environment using high-speed diffuse-light visualisation. The authors confirmed the correlation between the value of the non-dimensional energy barrier to nucleation,  $\chi$ , and the transition from mechanical to flash-induced atomisation. They demonstrated that the onset of the fully flashing regime occurs at a  $\chi$  value of around one. The same conclusion was reached by Lamanna et al. in [22], where a systematic study of flash atomization of standard and retrograde fluids using background illumination took place. Additionally, the authors reported the appearance of complex shock-wave structures at very high initial superheat. Finally, at the DLR facility, Lamanna et al. [12] investigated fully flashing LOx and ethanol sprays with the use of diffuse-light high-speed imaging. The authors demonstrated that the inception of flash boiling in cryogenic propellants requires a higher degree of superheat compared to storable propellants.

More recently, in the work of Rees et al. [23], the characteristic morphologies of the flash boiling LN<sub>2</sub> sprays like breakup patterns and spray angles were investigated with the use of high-speed shadowgraphy. Among the conclusions, the authors propose the introduction of a fourth breakup regime for highly superheated jets, the wide-flashing regime. In addition, in [24] a laser-based Phase Doppler system was set up to determine the spatial distributions of droplet velocities and diameters in highly superheated sprays. According to the authors, the

droplet diameter decreases with increasing injection temperature; however, the dependence of the droplet diameter on the injection temperature is less dominant for increasing injection pressures and the droplets are bigger at the same injection temperatures.

The scarcity of cryogenic-flashing experimental data makes the need for accurate and robust numerical methods to simulate the phenomenon imperative. An accurate numerical prediction of such two-phase flows can lead to a better understanding of the underlying flow and phase-change processes. In the case of injector orifices under flashing conditions, the fact that the rapid evaporation of the fluid has a tremendous influence on the characteristics of the resulting spray is overall supported by the experimental data. The importance of flashing for the evolution of sprays has been acknowledged in the area of gasoline direct injection (GDI) engines and the research is intense both in terms of experimental and numerical approaches [25,26]. Cryogenic flashing has also been investigated for cooling purposes [27] while studies on water, refrigerants, and light hydrocarbons have shown that in the case of in-nozzle flash evaporation, finer sprays, wider cone-angles and reduced penetration lengths compared to flows subdued to inertia-driven phase-change are observed [28]. Safety concerns for fuel applications [29] but especially with respect to aerospace and nuclear applications have led to further numerical investigations of flash boiling. The relevant cryogenic flow processes and, consequently the numerical methodology presented are also relevant to a wide range of other applications, ranging from gas liquefaction and desalination to cryosurgery and food freezing [30–33].

In cases of very rapid depressurisation, an initially sub-cooled liquid can transit to the, so called, *meta*-stable region, having a pressure equal to the respective saturation value, yet temperature higher than the respective saturation value. When in the metastable state, the system can remain stable for small fluctuations of the thermodynamic variables. However, due to the pressure disturbances, the metastable conditions cannot be maintained for a long time. The metastable liquid will overcome the energy barrier to nucleation and release its latent heat through the flash-evaporation process, finally evolving to the global minimum of free energy and reaching a new equilibrium stable state. Metastability effects play an important role in transient processes [34]. In nuclear safety analysis, flashing phenomena are present in the case of a loss of coolant accident (LOCA), as well as inducing flow instabilities in passive

safety systems driven by natural circulation. Liao and Lucas present the relevant advancements in the field in [35] and [34].

Nevertheless, not many numerical investigations highlighting the distinct characteristics of cryogenic sprays can be found in the open literature. In the work of Travis et al. [36], a theoretical two-phase model based on the Helmholtz energy EoS is developed. To account for the non-equilibrium effects, the homogeneous equilibrium model was modified and used for determining the critical flow rate for choked cryogenic flows. Lyras et al. [37] utilized the volume-of-fluid method coupled with the homogeneous relaxation model to investigate the flash boiling process and subsequent spray expansion of a liquid nitrogen flow through a throttle nozzle. Chen et al. [38] proposed a two-fluid numerical model that couples an interface area density model to the homogeneous relaxation model (HRM) for investigating the underlying physics of liquid nitrogen spray formation. In a numerical and experimental campaign to study flashing liquid nitrogen, Gärtner et al. [39] used a one-fluid approach, with tabulated thermodynamic properties and the HRM to account for phase change. In the recent works of Lureiro et al. [40,41] a multiphase solver based on the volume of fluid method and piecewise linear interface calculation (PLIC) reconstruction is used to perform direct numerical simulation) of the flash atomization of cryogenic LOx in the micro-scale and characterise the primary breakup regimes, as well as calculate the droplet-size distribution within the spray. Schmehl and Steelant [11] utilized an Eulerian-Lagrangian framework to simulate the pre-flow of nitrogen tetroxide (N<sub>2</sub>O<sub>4</sub>) oxidizer during the start-up of an upper-stage rocket engine. To account for the flash-induced expansion of the jet, an empirical flash atomization model was used. Ramcke et al. [42] used a similar numerical approach utilizing a simplified droplet flash evaporation model to investigate the pre-flow of LOx for satellite rocket engines. The aforementioned publications reveal that both cryogenic and storable flashing liquid sprays exhibit analogous characteristics, namely enhanced droplet atomisation, increased cone angle and acceleration of the compressible mixture.

The above review of the existing literature makes it clear that although effective approaches have been implemented to predict cryogenic liquid injection and flashing evaporation, the proposed methods are developed depending on specific thermodynamic conditions and application needs. Previous work by the authors in [43,44] has demonstrated the robustness of the technique in modelling phase-change and spray mixing in fuel-injection applications. To the authors' best knowledge, this is the first work in the open literature to propose and evaluate a universal modelling framework suitable for the prediction of multiphase, cryogenic wall-confined and unconfined spray-flow characteristics, for pressure outlet environments that range from near-vacuum to supercritical [45]. More specifically, a time-resolved, explicit, density-based solver implementing a Mach-number consistent numerical flux scheme has been developed and utilised. Thermodynamic properties of the operating fluids were computed by solving the Helmholtz energy Equation of State (EoS) and inserted in the numerical code in tabulated form. In the context of examining flash boiling during second-stage engine ignition, liquid oxygen has been selected as the operating fluid due to its extensive use as an oxidiser. To further evaluate the developed solver, liquid nitrogen was also considered due to the availability of experimental data for flash boiling conditions. In parallel with the developed density-based solver, a coupled (pressure-based) solver utilising a kinetic-theory-based model is examined to comparatively assess the accuracy of numerical predictions produced with the use of diverse phase-change modelling approaches.

This universal methodology based on tabulated thermodynamics, that is applicable to a wide range of superheat levels, is presented in a comparative manner against the Hertz-Knudsen kinetic-theory-based mass transfer model and validated against relevant experimental data. This phase-change model can be calibrated to model flash evaporation for various superheat levels and therefore produce accurate results; however initial calibration data must be available. The use of a

thermodynamic table with real-gas thermodynamic properties produces accurate results for high superheat values while capturing the process with satisfactory accuracy for lower values of superheat. The advantage of the tabulated methodology is that after the initial table of fluid properties is created for a range of conditions, no calibration is needed since the phase change rates are dictated by the tabulated real-gas thermodynamics. Therefore, the tabulated approach can be a flexible methodology to be used when examining a specific fluid for a wide range of conditions or different geometries. Overall, this investigation aspires to clarify the effectiveness of the two aforementioned approaches in simulating cryogenic flows of liquid oxygen and nitrogen under extreme flash boiling, near-vacuum conditions.

## 2. Numerical methodology

Two flow solvers have been employed in the present investigation, i. e., an implicit coupled pressure/velocity solver (nominally referred to from now on as 'pressure-based') and an explicit density-based solver. The basic set of governing equations solved in both cases comprised the continuity, momentum and energy conservation equations, the fundamental formulations of which can be found in the work of Karathanassis et al. [46] and are summarised below.

$$\frac{\partial(\rho_{mix})}{\partial t} + \nabla(\rho_{mix} \vec{u}) = 0 \quad (1)$$

$$\frac{\partial(\rho_{mix} \vec{u})}{\partial t} + \nabla(\rho_{mix} \vec{u} \vec{u}) = -\nabla p + \nabla[\mu_{mix}(\nabla \vec{u} + \nabla \vec{u}^T)] \quad (2)$$

$$\frac{\partial \sum_{i=1}^2 (\alpha_i \rho_i E_i) + \nabla \sum_{i=1}^2 (\alpha_i \vec{u} (\rho_i E_i + p))}{\partial t} = \nabla(k_{mix} \nabla T), \quad (3)$$

$$E_i = h_i - \frac{p}{\rho_i} + \frac{u_i^2}{2}$$

In Eqs. (1) to (3),  $\rho$  denotes density,  $\vec{u}$  is the velocity vector,  $t$  for time,  $p$  represents the pressure field and  $\mu$  is the fluid viscosity. The volume fraction of each phase is  $\alpha$ ,  $k$  denotes the thermal conductivity of the two-phase fluid,  $T$  stands for temperature and finally,  $h$  is the sensible enthalpy. The index "mix" corresponds to the mixture and "i" to a specific phase of the mixture. The complete numerical methodologies, along with the sets of equations solved have been described in more detail in previous works of the authors' group, specifically in the work of Karathanassis et al. [46] regarding the pressure-based solver and Kyrizakis et al. [47,48] regarding the density-based solver.

With respect to the coupled (pressure-based) solver, a two-phase mixture approach was implemented, including an additional equation for the vapour transport, as outlined in the following section. Numerical schemes with 2nd-order accuracy were employed for the discretisation of the governing equations. More specifically, the QUICK scheme was employed for the discretisation of the vapour-fraction equation, while a second-order upwind scheme was used for density interpolation, as well as for the discretisation of the momentum and turbulence transport equations. An implicit second-order backward differencing technique was used for time integration with a time step value of  $10^{-8}$  s, resulting in a CFL-criterion value smaller than 1 in the entire computational domain for all the pressure-based solver simulations. Solution for each time step was deemed as converged, once the residuals for the set of governing equations employed by the solver dropped by at least three orders of magnitude.

In the case of the density-based solver, a single-fluid modelling approach has been formulated and the 3-D RANS equations in conservative form were considered. In essence, an infinite phase-change rate was assumed at the bubble interface, i.e., the establishment of thermodynamic equilibrium, and the entire process was replicated by an appropriate EoS (refer to Section 2.2). The interphase temperature in the present investigation is taken as equal to the local cell temperature, which is calculated by the solution of the energy equation.

Thermodynamic non-equilibrium and its effects play an important role in flashing conditions during highly transient processes with abrupt pressure gradients [34]. All the examined cases, however, reach a quasi-steady solution. The thermal equilibrium assumption, imposed by the density-based solver can, therefore, produce accurate results, as also demonstrated for cryogenic fluids in [45]. Additionally, it should be noted that the pressure-based solver calibration yielded an accommodation coefficient value of  $\lambda = 1$ , suggesting close-to-equilibrium thermodynamic conditions. Since the Mach number is probable to obtain highly different values in the pure liquid, vapour and two-phase mixture regions, a Mach-number consistent numerical flux has been implemented based on the HLLC and the AUSM fluxes [49,50]. Conservative variables at cell interfaces, required for the calculation of the fluxes, were determined using the MUSCL-Hancock reconstruction [51], 2nd-order accurate in space. A 4th-order accurate, four-stage Runge-Kutta method has been selected for time integration, with a CFL criterion of 0.1 imposed for all the density-based explicit solver simulations performed. Again, the solution for each time step was deemed as converged, once the residuals for the set of governing equations employed by the solver dropped by at least three orders of magnitude.

### 2.1. Mass-transfer model

As mentioned, a two-phase mixture model was employed in the coupled, pressure-based solver to capture the phase-change process under flash-boiling conditions. Mechanical equilibrium, i.e., a common velocity field, was also assumed for the two phases. Regarding the liquid phase, compressibility was imposed with the use of Tait EoS using a reference density of  $1022.1 \text{ kg/m}^3$  at  $p = 17 \text{ bar}$ ,  $T = 113 \text{ K}$  for LOx and a reference density of  $782.86 \text{ kg/m}^3$  at  $p = 4 \text{ bar}$ ,  $T = 82.5 \text{ K}$  for LN<sub>2</sub>. The respective vapour phases were treated as ideal gases. The reference values of latent heat of evaporation were taken equal to  $185.25 \text{ kJ/kg}$  for LOx at a temperature of  $113 \text{ K}$  and  $192.19 \text{ kJ/kg}$  for LN<sub>2</sub> at a temperature of  $82.5 \text{ K}$ . Energy transfer between liquid and vapour phases was calculated based on reference latent heat values, the integration of heat capacity of each fluid for a temperature range and on the calculated phase-change rate. The set of governing equations for the mixture was complemented by an advection equation for the conservation of the vapour phase volume fraction as follows:

$$\frac{\partial(a_v \rho_v)}{\partial t} + \nabla \cdot (a_v \rho_v \vec{u}) = \dot{R} \quad (4)$$

where the phase-change rate  $\dot{R}$  corresponds to flash vaporization. For the simulations conducted in this study, the rate was calculated from the Hertz-Knudsen equation derived from the kinetic theory of gases [52]:

$$\dot{R} = \frac{\lambda A_{int} (p_{sat} - p)}{\sqrt{2\pi R_g T_{int}}}, A_{int} = n^* 4\pi r^2 \quad (5)$$

where  $R_g$  and  $T_{int}$  are the ideal-gas constant and the bubble-interphase temperature respectively, while  $A_{int}$  is the overall vapour interface surface area, which is calculated assuming a nucleation-site density  $n = 10^{16} \text{ sites/m}^3$  and a bubble radius of  $r = 10^{-6} \text{ m}$ . The nucleation site density was calibrated based on the maximum spray cone angle, while the bubble radius has been deemed as representative of flashing-flow propagation in different benchmark geometries. In fact, along with an accommodation coefficient  $\lambda$  value of 1.0, they are indicative of thermodynamic conditions approaching equilibrium [46]. Since a mixture model is employed, the interphase temperature is taken as equal to the local grid cell temperature provided by the solution of the energy equation. The degree of deviation from thermodynamic equilibrium is reflected in the value of the accommodation coefficient  $\lambda$ . Values of either 1.0 or 0.1 correspond to conditions similar to thermodynamic equilibrium and strongly deviating from it, respectively [53]. The capability of the Knudsen-based mass-transfer model to capture the

phase-change rate in flashing flows has been demonstrated in [46] and has also been implemented in CFD software [54] in order to investigate flash boiling in gasoline fuel injector nozzles.

### 2.2. Helmholtz energy equation of state

LOx and LN<sub>2</sub> thermodynamic properties required by the density-based solver are derived from the Helmholtz energy EoS. The table containing the LOx properties is calibrated within the temperature range  $54.4 \text{ K} \leq T \leq 500.0 \text{ K}$ , for a maximum density of  $\rho_{\max} = 1400.5 \text{ kg/m}^3$ . For LN<sub>2</sub> the thermodynamic properties are tabulated for a temperature range of  $63.2 \text{ K} \leq T \leq 329.8 \text{ K}$ , for a maximum density value of  $\rho_{\max} = 1100.0 \text{ kg/m}^3$ . The properties are organised into a thermodynamic table that may include a wider or narrower range of values, depending on the application. The dimensionless form of the aforementioned EoS for the Helmholtz energy  $a$ , having as independent variables the density and the temperature [55] is:

$$\frac{a(\rho, T)}{RT} = a(\delta, \tau) = a^0(\delta, \tau) + a^r(\delta, \tau) \quad (6)$$

where  $\delta = \rho/\rho_c$ ,  $\tau = T_c/T$ ,  $a^0$  is the dimensionless Helmholtz energy of the ideal gas and  $a^r$  is the residual Helmholtz energy. The last two variables,  $a^0$  and  $a^r$  can be determined as reported by Kyriazis et al. in [39]. Eq. (6) can then be used to determine pressure, internal energy, enthalpy and speed of sound of the fluid as a function of density and temperature. The saturation curve is identified using Maxwell's criterion. Properties within the saturation dome, are determined using a mixture assumption and the mixture's speed of sound is calculated using the Wallis speed-of-sound formula [45].

Due to the considerable computational cost that solving the Helmholtz EoS at each time step entails, a tabulated-data technique, similar to the one proposed in [56] has been employed. The procedure and table development has been performed for each substance of interest. Two structured thermodynamic grids of approximately  $10 \times 10^4$  and  $7 \times 10^4$  elements have been created, one for each working fluid, namely LOx and LN<sub>2</sub>, containing information for all the thermodynamic properties on each thermodynamic node defined by a density and internal energy value. For LOx cases, the density range of the grid is  $0.125 \leq \rho \leq 1400.5 \text{ kg/m}^3$  divided into 251 points of fixed  $\Delta\rho = 5.055 \text{ kg/m}^3$ , while the internal-energy range of the grid is  $-171.14 \leq e \leq 165.51 \text{ kJ/kg}$  divided into 400 points of fixed  $\Delta e = 0.84161 \text{ kJ/kg}$ . For LN<sub>2</sub> cases, the density range of the grid is  $0.01 \leq \rho \leq 1100.01 \text{ kg/m}^3$  divided into 221 points of fixed  $\Delta\rho = 5.0 \text{ kg/m}^3$ , while the internal-energy range of the grid is  $-169.50 \leq e \leq 129.5 \text{ kJ/kg}$  divided into 300 points of fixed  $\Delta e = 1.0 \text{ kJ/kg}$ . The variation of pressure and internal energy of nitrogen as a function of density and temperature is presented in Fig. 1. The surfaces have been produced by employing the aforementioned tabulating procedure. The saturation curves are represented as black dashed lines.

Once density and internal energy are calculated by the RANS equations, the corresponding element of the thermodynamic table is identified through numerical inversion from the above quantities. Any thermodynamic property  $\phi$  of the table is then approximated by a finite element bilinear interpolation:

$$\phi(\rho, e) = \sum_n^{nodes} N_n(\rho, e) b_n \quad (7)$$

where  $\phi$  corresponds to the pressure, temperature or speed of sound, required for the calculation of the fluxes in the density-based solver. Full details on the shape functions  $N$  employed and the calculations of unknowns  $b$  on each node  $n$  are reported in [47].

### 2.3. Turbulence closure

All the simulated cases are characterized by high Reynolds numbers ranging from  $8.7 \times 10^7$  to  $16.2 \times 10^7$ . The flow of cryogenic fluids



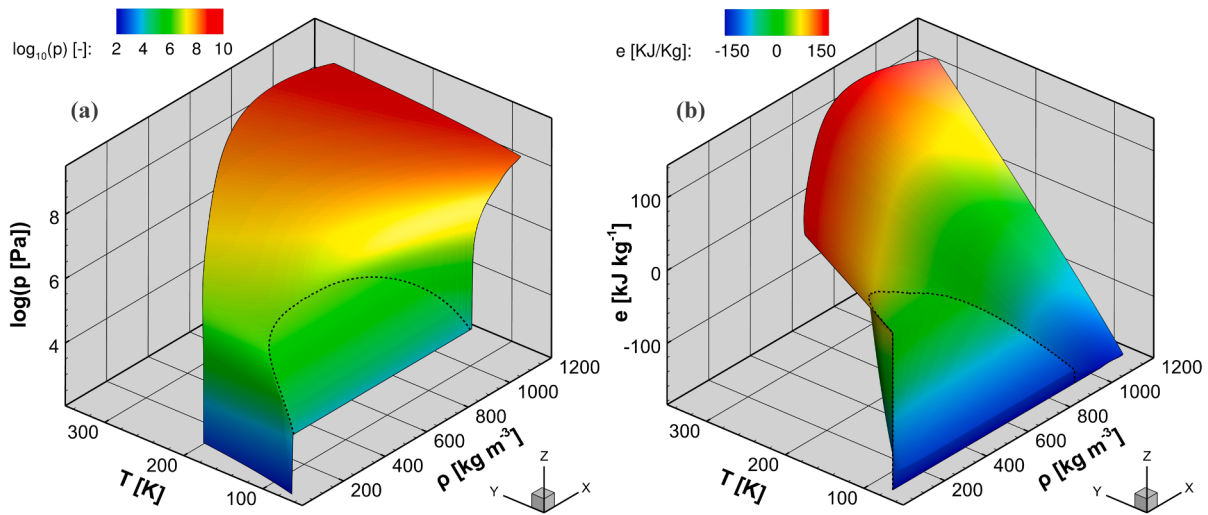


Fig. 1. Three-dimensional phase diagrams for nitrogen: (a) pressure and (b) internal energy in terms of density and temperature.

developing through the selected orifices has therefore been found to be within the turbulent regime for all cases. For the calculation of Reynolds numbers, the diameter of each orifice was used as the characteristic length scale, while an approximation of the velocity was made based on experimental values of the mass flow rate. Finally, liquid phase prop-

erties at the injection pressure and temperature have been assumed for the Reynolds calculations. To account for contributions to the viscosity  $\mu$  and thermal conductivity  $k$  due to turbulence effects, the  $k-\omega$  Shear Stress Transport (SST) turbulence model was employed since the specific turbulence model has been demonstrated to perform well in highly

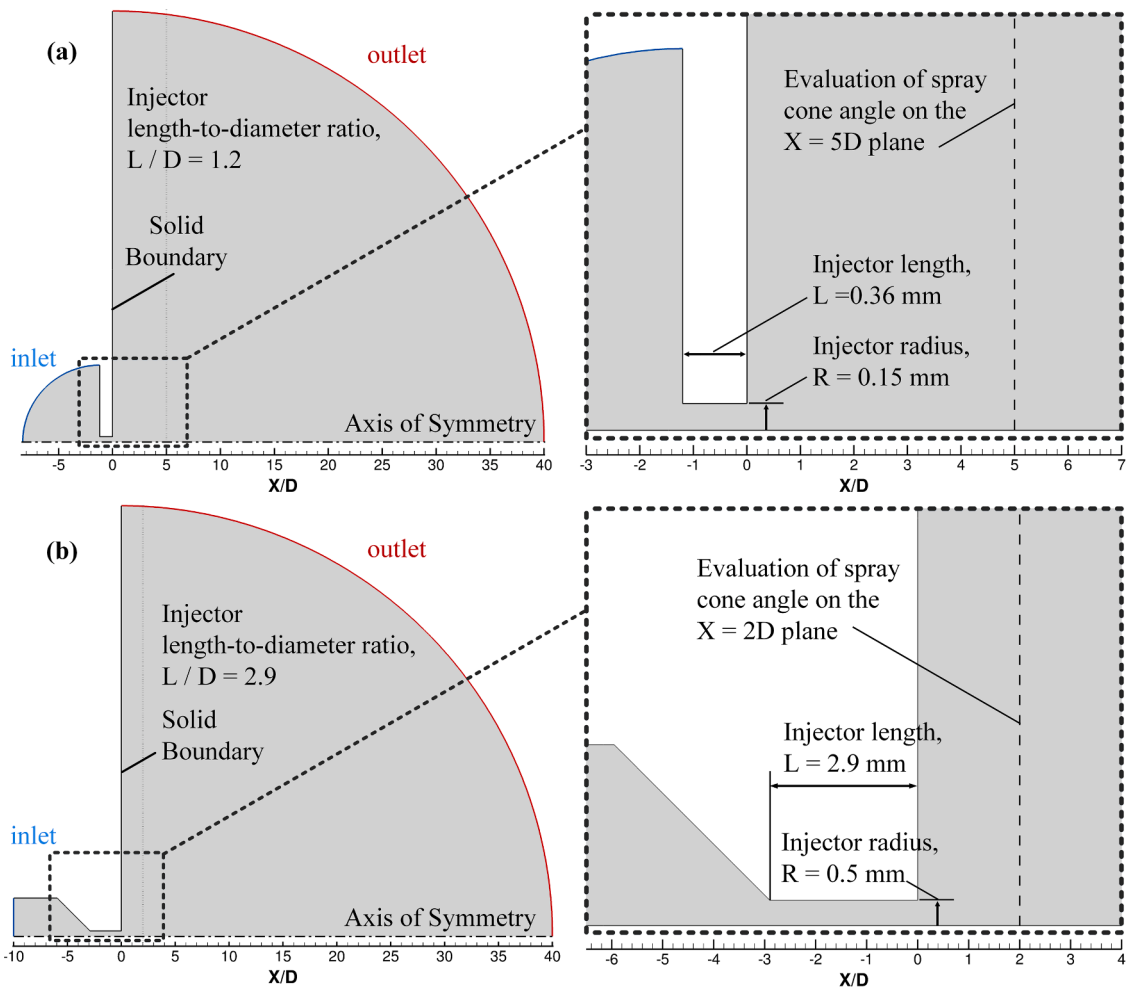


Fig. 2. Geometry of (a) liquid oxygen injector (injector A) employed in [12] and (b) liquid nitrogen injector (injector B) employed in [24]. The panels represent the numerical domain used for the simulation. The outflow part extends downstream the injector exit to a length equal to 40 orifice diameters.

turbulent wall-bounded flows, where secondary flow is also possible to arise. More specific, the SST formulation exhibits a  $k-\epsilon$  behaviour in the free-stream without suffering by excessive turbulence production in regions of recirculation [57]. The model is suitable for adverse pressure gradients that are present near the injector's exit hole [39] and has performed better than the  $k-\epsilon$  regarding mass flow results in the context of superheated nozzle flows [37]. Standard wall functions were utilised for near-wall turbulence treatment. The respective  $y^+$  values for the numerical grid employed for the simulations were of the order of 10.

#### 2.4. Domain discretisation

Two geometries are represented in this study referred to as injector A and injector B. Injector A is a typical cylindrical LOx injector of 0.36 mm length and constant diameter of 0.30 mm and presented in Fig. 2a. The specific injector geometry has been used for obtaining the experimental data available from Lamanna et al [12]. Injector B is a cylindrical LN<sub>2</sub> injector of 2.9 mm length and a constant diameter of 1 mm, utilized in the experimental campaign of Rees et al. [24] and is presented in Fig. 2b.

Since both orifices are axisymmetric, both domains were reduced to a wedge produced by rotating the nozzle layout, around the symmetry axis by 5° as depicted in Fig. 3. As can be seen in the same figure, the inflow section has been expanded upstream in both domains to impose the stagnation conditions of the experiments. After the grid independence study presented in paragraph 2.6, numerical grids of approximately 26,000 and 50,000 cells were employed to represent injectors A and B, respectively, with comparable cell density in the in-nozzle and spray-outlet regions for both geometries. The developed numerical grids

were primarily structured comprising more than 97 % hexahedral cells. Regarding the injector hole, the spatial discretisation for both injectors was 50 cells through the cross section. The near-wall region in each case was refined with the use of 12 inflation layers with a growth factor of 1.2. The grids resulted in  $y^+$  values of the order of 10, suitable for turbulence modelling using RANS.

#### 2.5. Boundary and initial conditions

The set of boundary conditions imposed in the examined cases replicate the physical conditions prevailing during the actual LOx and LN<sub>2</sub> experiments presented in [12] and [24]. Appropriate constant values of static pressure were imposed at the inlet and outlet of the domain in accordance with the experimental conditions. A zero-gradient condition was imposed for the boundary-normal velocity component at the inlet, while the remaining velocity components were set to zero. At the outlet boundary, zero-gradient boundary conditions were set for all velocity components and all the transported quantities. A no-slip condition was imposed on all the surfaces acting as orifice walls that were also treated as adiabatic. Regarding energy-conservation considerations, a constant temperature value in the case of the pressure-based solver and a constant internal energy value in the case of the density-based solver were imposed on the domain inlet and outlet according to the equation formulations implemented in each solver.

Regarding initialization, in the cases of the pressure-based solver, a Laplace-based equation was solved to establish an initial pressure field while quiescent fluid was assumed at the initial time instance. For the density-based solver, a solution produced by the SIMPLE solver was used for the initialization of the pressure and velocity fields. All simulations

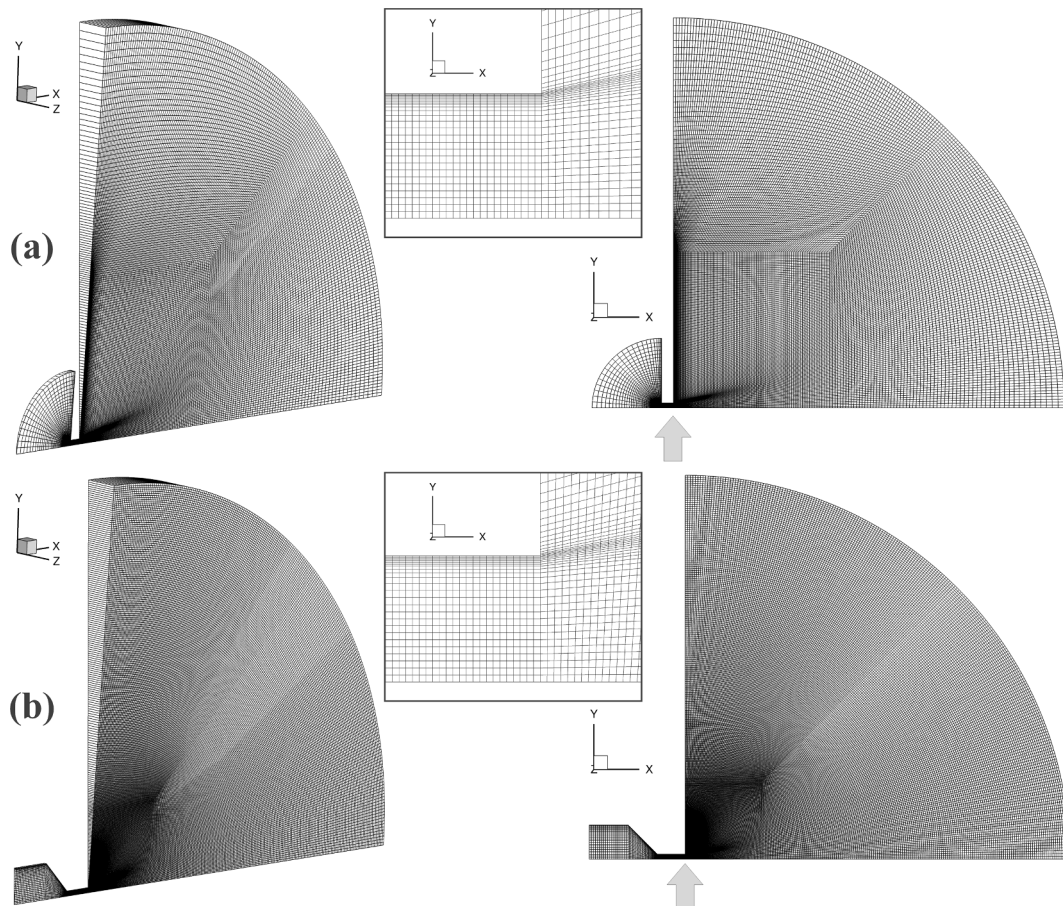


Fig. 3. Views of the numerical grid of (a) the LOx injector and (b) the LN<sub>2</sub> injector including a focused view of the location around the exit of each injector (as indicated by the vertical arrow).

were initialized assuming pure liquid in the inlet and nozzle volume, while the gas phase was assumed to fill the downstream diverging volume. Finally, temperature values were set equal to the respective inlet values throughout the domain. Table 1 summarizes the set of boundary and initial conditions applied to all examined cases.

### 2.6. Validation and grid independence

The pressure-based solver employing the Hertz-Knudsen phase-change model has been extensively validated with reference to internally and externally flashing flows considering water as the working medium in previous works of the authors, see [45,46]. Specifically, the model has been demonstrated to accurately capture phase-change in a converging-diverging nozzle, a (throttle) nozzle with an abrupt contraction and a rapidly depressurising duct (pipe blow-down). Furthermore, the density-based algorithm has been validated in previous works with reference to bubble- [47], and droplet-dynamics [58] simulations, while the accuracy of the tabulated technique based on the Helmholtz energy EoS has been verified in reference to the properties of n-dodecane [47]. In a different study, an additional validation study was set up in order to further evaluate the capability of the density-based solver to capture LOx flows using the Helmholtz EoS thermodynamic closure. The relevant predictions are presented in detail in [45].

In order to ensure the independence of the RANS numerical solution from the density of the numerical grid, three different grids of increasing cell count were created to represent the geometry of injector A, consisting approximately of 10, 26 and  $107 \times 10^3$  cells. The pressure-based solver was utilized to simulate case 3 of Table 2 for the grid independence study, a case with high superheat where severe expansion and large spray cone angles were expected. The results produced by the three numerical grids are presented in Fig. 4, in terms of pressure and vapour volume fraction distributions along the orifice symmetry axis.

Due to the fact that the resulting flow field reaches quasi-steady state conditions, the flow variables are time-averaged over a period of 20 ms, initiating after an initial transient period of around 4 ms. The results presented in Fig. 4 reveal that all used grids can qualitatively capture the overall flow characteristics. The intermediate grid has been adopted for all following simulations, as the results produced with said grid were of comparable accuracy to those of the dense grid, with negligible discrepancies, yet with reduced computational load. A numerical grid of similar topology consisting of 51,856 cells has been employed for Injector B, with comparable cell density both in in-nozzle and spray regions.

### 3. Results

The test cases examined in this study are summarised in Table 2. Specifically, cases 1 to 4 refer to LOx flow and correspond to the experimental conditions and the resulting spray cone angles reported by Lamanna et al. [12], whereas cases 5 to 10 refer to LN<sub>2</sub> flow and

**Table 1**  
Summary of boundary and initial conditions imposed for the numerical simulations.

Boundary Conditions	Inlet	Outlet	Wall
Pressure-based	$p = p_{in}$ $T = T_{in}$	$p = p_{out}$ $T = T_{out}$	$\vec{u} = 0$ $\partial T / \partial n = 0$
Density-based	$p = p_{in}$ $e = e_{in}$	$p = p_{out}$ $T = T_{out}$	$\vec{u} = 0$ $\partial T / \partial n = 0$
<b>Initial Conditions</b>			
Both solvers	$T = T_{in}$	$a_{inlet} = 0, a_{orifice} = 0, a_{outlet} = 1$	
Pressure-based	$p = p_0$	$\vec{u} = 0$	
Density-based	$p = p_0$	$\vec{u} = \vec{u}_0$	

**Table 2**

List of examined test cases, including the operating fluid, boundary conditions and superheat  $R_p = p_{sat}(T_{in}) / p_{out}$  for each case.

Case	Fluid	$p_{in} \cdot 10^5$ [Pa]	$p_{out}$ [Pa]	$T_{in}$ [K]	Superheat $R_p$ [-]
1	LOx	17	20,600	113.0	33
2		17	14,140	113.0	48
3		17	9100	113.0	74
4		17	2750	113.0	245
5	LN <sub>2</sub>	8	58,020	82.5	3
6		8	24,870	82.5	7
7		8	6130	82.5	28.4
8		4	58,020	82.5	3
9		4	24,870	82.5	7
10		4	3330	82.5	52.3

specifically the experimental campaign of Rees et al. [24] for which data regarding mass flow rates and spray cone angles are available. The rationale for selecting the aforementioned cases was to test the applicability of the methodologies presented in this study for a wide range of boundary conditions and for two different cryogenic fluids. Moreover, the juxtaposition of the results from specific cases provided useful insight into the flash evaporation process. Transient simulations have been performed for all cases, yet it was confirmed that the respective flow and temperature fields reached to steady-state (or quasi-steady-state) solutions in all cases; thus, the time-averaged flow and temperature fields are presented.

Due to the fact that the tested temperature and pressure conditions can lie below those of the triple point of LOx and LN<sub>2</sub>, there is indeed a possibility of solidification of the operating fluids. Nevertheless, in the work of Lamanna et al. [12] (cases 1 to 4 of Table 2), no reports of solidified LOx are found. In the case of fully-flashing LN<sub>2</sub> sprays of Rees et al. [24] (cases 7 and 10 of Table 2) flakes of solidified nitrogen were indeed observed close to the walls of the vacuum chamber and therefore away from the active visualisation region. Since the current investigation is mainly oriented towards aerospace applications, where icing is to be avoided, a simple limiter was set in the energy equation to avoid temperatures below solidification. It was confirmed that this limiter did not interfere with the robustness and the accuracy of the solution process.

#### 3.1. Liquid oxygen flashing flow

The numerical results corresponding to cases 1 to 4 of Table 2 are discussed in this section. In this specific set of cases, LOx is used as the working fluid and the imposed boundary conditions are chosen to result in an increasing superheat. Experimental data are available for comparison from the experimental campaign of Lamanna et al. [12] where the spray cone angle of flashing LOx was measured at a distance equivalent to 5 nozzle diameters downstream of the nozzle's exit.

Fig. 5 summarizes the results produced by the two approaches and evaluates the predictive capability of the two methods in terms of spray cone angle, for superheat ranging from 33 to 245. In accordance with the experimental spray cone-angle measurements, the angle is measured at a distance equivalent to 5 nozzle diameters after the nozzle's exit, as can be seen in the inset of Fig. 5. Since no manufacturing asymmetries or irregularities can be explicitly captured numerically, the numerical data only correspond to half of the diverging layout downstream of the injector outlet and the angle value is then doubled. Fig. 5 showcases the differences in the behaviour of the two algorithms in terms of phase-change modelling.

The Hertz-Knudsen phase change model can be calibrated to model flash evaporation for various degrees of superheat. In the literature, the model has been used for closed geometries and lower superheat with a nuclei density value of  $10^{13}$  and has produced accurate results [45]. In this numerical campaign, the model was properly calibrated based on the maximum spray cone angle parameter in order to qualitatively

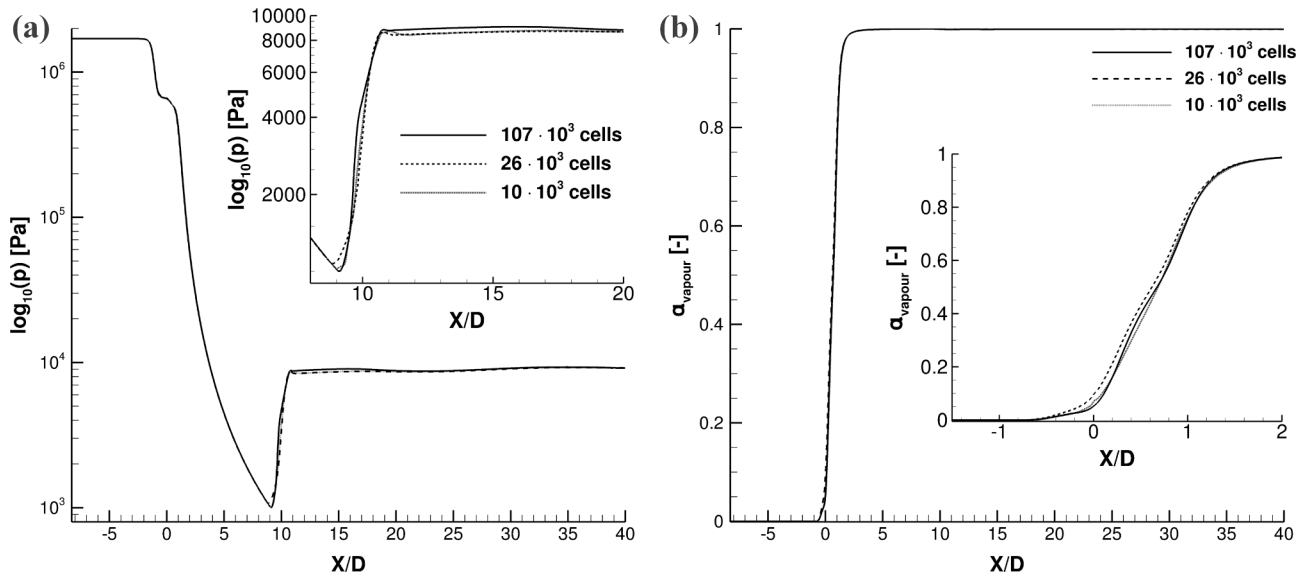


Fig. 4. Grid independence analysis of the numerical solution: (a) Pressure and (b) vapour volume fraction distributions at the orifice symmetry axis for three numerical grids of increasing cell number.

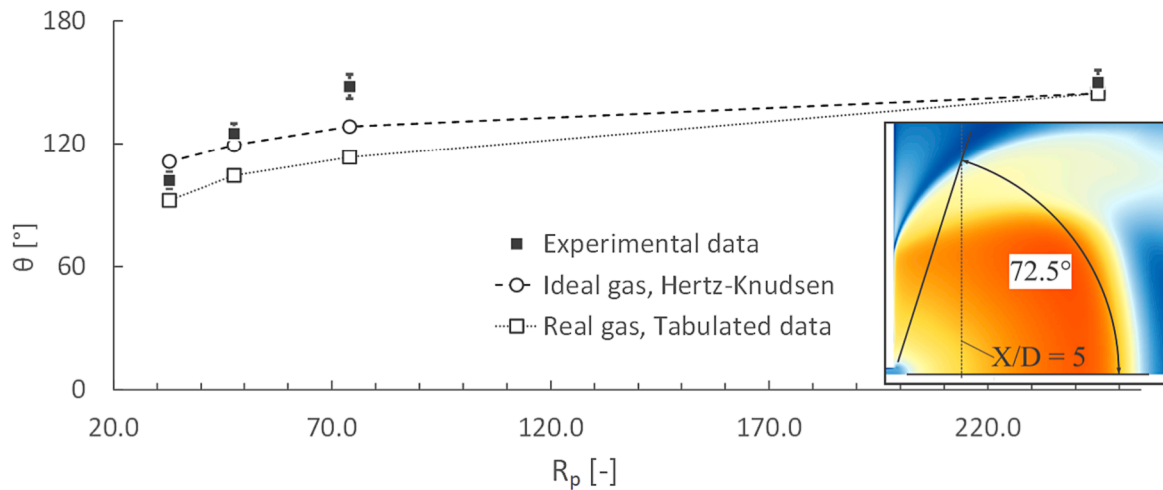


Fig. 5. Oxygen spray cone angle for an inlet pressure of 17 bar and variable LOx injection conditions of increasing superheat. Conditions correspond to cases 1 to 4 of Table 2. Spray cone angles measured at a distance equivalent to 5 nozzle diameters downstream the nozzle (see figure inset).

capture an intense flashing process, unrestricted by wall boundaries, and the bubble nuclei density was set to  $10^{16}$  for all examined cases. The second method employing a thermodynamic table with real-gas thermodynamic properties produces equally accurate results for high LOx superheat (case 4) while capturing the process with satisfactory accuracy for lower superheat ratios. The advantage of this method is that, after the initial table of fluid properties has been created for a range of conditions, no calibration is needed, since the phase change rates are dictated by the tabulated real-gas thermodynamics. Therefore, between this numerical campaign and the LOx campaign presented in [45], no changes were needed in terms of the thermodynamic table used, which demonstrates the applicability of the specific approach regardless of the boundary conditions or the geometry used.

Fig. 6 presents a comparison between the two approaches in terms of pressure, velocity, density and temperature fields for a case of  $R_p = 245$ . Comparing the pressure fields (Fig. 6a), the two solvers are demonstrated to be in good agreement, as it is clear that the pressure decreases in a similar manner. The velocity, density and temperature contour plots reveal the formation of bell-shaped Oxygen spray with an

almost identical spray cone angle on the measurement location ( $X[m] = 5 \times \text{Nozzle diameter}$ ). Although the pressure decrease that takes place is similar for both approaches, the use of tabulated thermodynamics with the density-based solver imposes an infinite phase-change rate that affects the temperature ranges of the expanding flow after the nozzle exit (Fig. 6d). The density-based (tabulated) solver predicts, therefore, the presence of an area of lower temperature and comparable but slightly higher density (Fig. 6c) than the pressure-based solver. Those changes in the density affect the maximum velocity that the expanding flow reaches (Fig. 6b), before decelerating and adjusting to the ambient pressure with a steep gradient. The evolution of the field-variables values along the axis of symmetry further supports the aforementioned findings and is presented in Fig. 7.

The comparison between the pressure-based solver ( $R_p = 245(PB)$ ) and the density-based solver ( $R_p = 245(DB)$ ) curves of Fig. 7 reveals the characteristic features of the flash evaporation process and the differences between the two approaches. For those curves, the pressure and velocity fields (Fig. 7a and Fig. 7b) share the location where the minimum and maximum values are reached, approximately 15 nozzle diameters downstream of the nozzle exit. Regarding the pressure-based



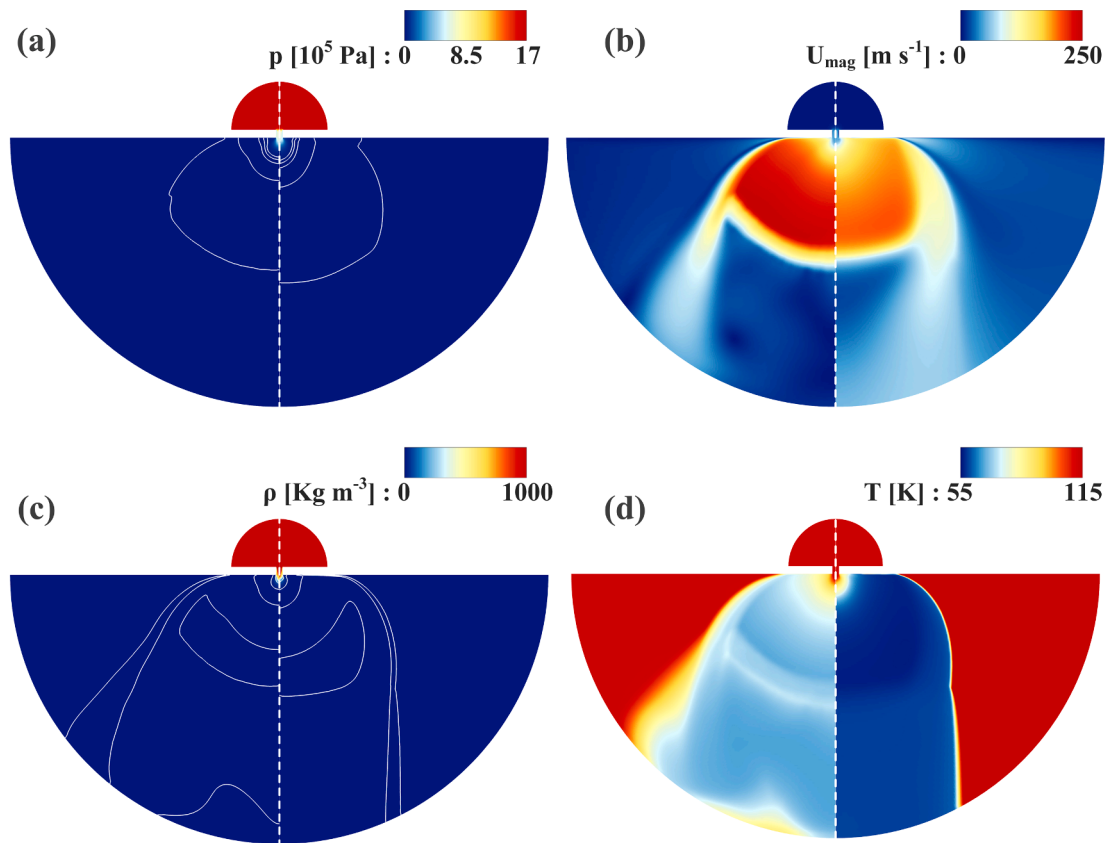


Fig. 6. Contour plots of (a) pressure, (b) velocity magnitude, (c) density and (d) temperature variable distribution for case 4 of Table 2. Pressure-based solver results are presented on the left of each subplot while density-based solver results are on the right.

solver, the pressure decreases in a marginally steeper fashion and the maximum velocity value is almost 25 % greater in comparison to the density-based solver. This difference in maximum velocity values emanates, predominantly, from the density field (Fig. 7c), which adjusts the speed of sound in the orifice. Regarding the temperature fields (Fig. 7d), the phase change mechanisms play a key role in the behaviour of the quantity. In the case of the density-based (tabulated) solver, higher (infinite) phase change rates lead to higher energy absorption which results to lower temperatures.

Examining the results of Fig. 7 in terms of increasing  $R_p$  ( $R_p = 33, 48, 74$  and  $245(PB)$ ), reveals that the pressure and density fields (Fig. 7a and Fig. 7c) are exhibiting similar variations after the nozzle exit. A steep initial decrease after the  $X/D = 0$  point and an equally sharp gain that reinstates the variable value to match a final equilibrium value. The higher the superheat level, the further from the nozzle exit the increase of pressure and density will take place, and the lower the equilibrium value will be. Temperature profiles (Fig. 7d), reveal their decrease due to the intense evaporation process and the absorption of latent heat. On the location where the flow expansion stops, a static (over time) shockwave is formed; an amount of vapour undergoes condensation, and a local increase in the temperature is observed. Finally, regarding the axial velocity (Fig. 7b), a flow-recirculation region can be discerned for the cases of lower superheat (cases 1 to 3), as negative axial velocity values prevail between approximately 10 to 15 nozzle diameter lengths past the location of the injector exit. The recirculation can be attributed to shear forces from the flow surrounding the spray core. For the cases of higher superheat, the expansion is more extended and the surrounding flow is located further away from the spray axis, thus limiting the shear effects on the axial velocity value over the symmetry axis.

Fig. 8 presents contour plots of the flow and temperature fields for cases 1 to 4 of Table 2 in a manner of increasing superheat level. Distinct

topologies common for all cases can be identified. Regarding the pressure field (Fig. 8a) a hemispherical volume of steep pressure gradients forms immediately after the nozzle exit, followed by a region (Marker “1”) where pressure obtains values lower than the outlet pressure.

This particular area becomes more extensive with increasing degree of superheat. For instance, for  $R_p = 245$ , it reaches up to a length of 20 nozzle diameters downstream the nozzle exit. Likewise, the velocity field (Fig. 8b) reveals a hemispherical zone of fluid acceleration, or, in other words, flow expansion (Marker “2”), where supersonic velocity values are reached. The expansion stops at the location where pressure recovers in an abrupt manner, i.e., a shockwave forms. From an overall-topology standpoint, a bell-shaped spray forms that encloses the annotated areas. The flow velocity at the boundaries of the spray is higher than the core where recirculation zones (Marker “3”) form in the wake that is created downstream of the pressure discontinuity due to shearing induced by the high-velocity periphery. Besides, the density field (Fig. 8c) closely follows the pressure field, with the regions of low fluid density (Marker ‘4’) corresponding to regions of low pressure as well. The proximity to the injector’s outlet of this low density/pressure location (Markers “1” and “4”) is a function of superheat. The higher the superheat, the further from the injector’s exit is the density/pressure minima located. Finally, temperature decreases within the spray area (Fig. 8d), as expected due to the evaporation of LOx and the absorption of latent heat. The higher the  $R_p$  the lower the minimum temperature. For all cases, there is a region where temperature briefly increases as condensation takes place after the pressure recovery (Marker ‘5’).

### 3.2. Liquid nitrogen flashing flow

The numerical results corresponding to cases 5 to 10 of Table 2 are discussed in this section. In the specific set of cases,  $LN_2$  is used as the

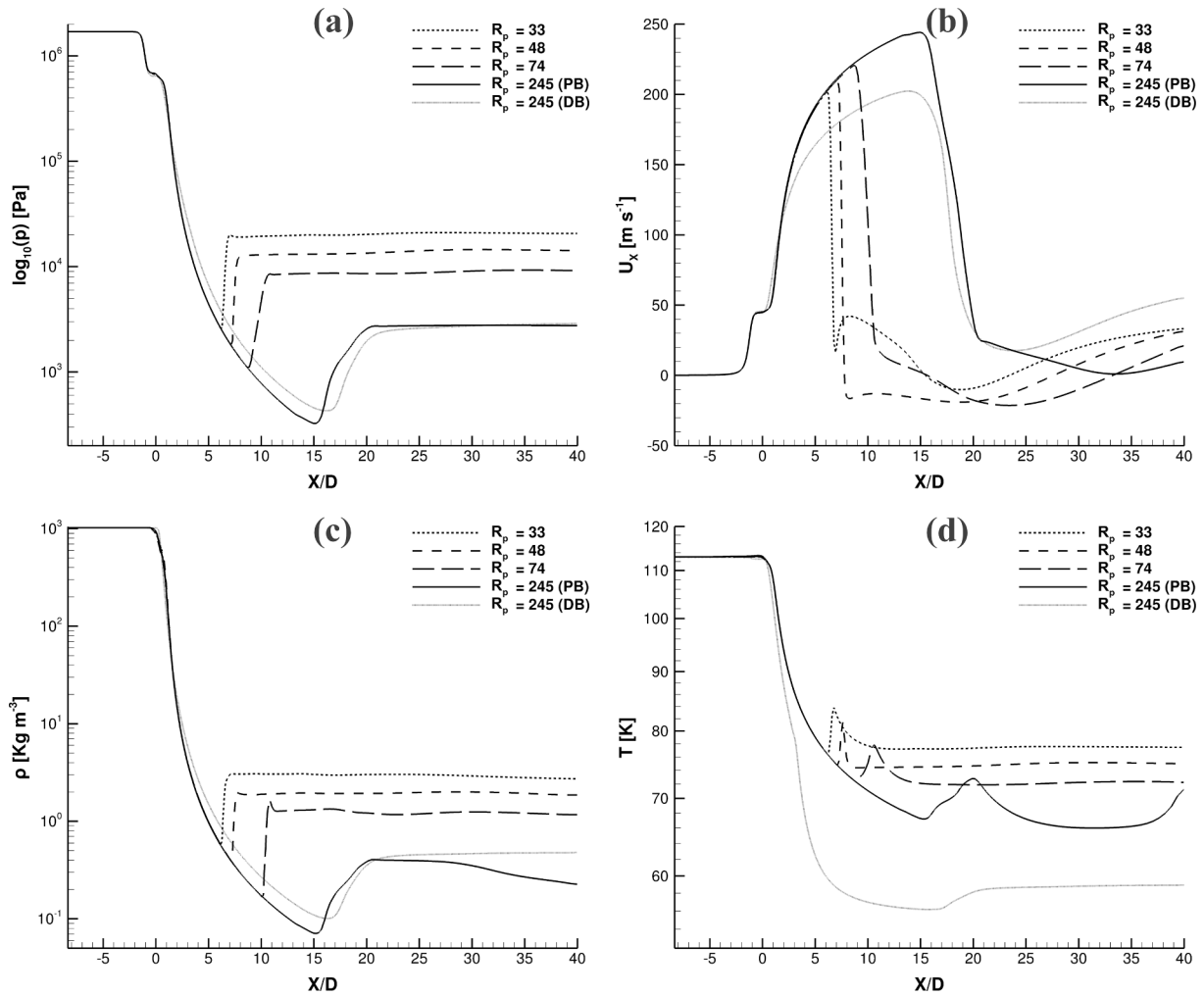


Fig. 7. Distribution of (a) pressure, (b) axial Velocity, (c) density and (d) temperature along the nozzle axis of symmetry as predicted by the two solvers for case 4 of Table 2 and by the pressure-based solver for cases 1 to 3 of Table 2. PB and DB stand for the pressure and density-based solvers.

working fluid and the imposed boundary conditions are chosen to result in an increasing superheat level for two values of inlet pressure. Experimental data are available for comparison from the campaign of Rees et al. [24], where in-nozzle mass flow rates and spray cone angles of flashing LN<sub>2</sub> were measured. Table 3 presents the comparison between the experimental measurements and the numerical data produced using the two solvers tested. As can be seen, good agreement between experiments and predictions has been achieved, with the density-based solver outperforming the respective pressure-based in terms of accuracy owing to its independence from tuning parameters.

Fig. 9 summarizes the results produced with the two approaches and their predictive capability is evaluated in terms of spray cone angle, for two different values of inlet pressure, namely 8 (Fig. 9a) and 4 bar (Fig. 9b), respectively. As demonstrated by Fig. 9a, both numerical methods exhibit high accuracy in terms of spray cone angle for cases of higher inlet pressure (5 to 7 of Table 2). For the lower inlet-pressure counterparts (cases 8 to 10 of Table 2) the numerical results match perfectly the experimental values of the spray-cone angle for a high level of superheat. For  $R_p = 7$  both methods seem to underestimate the cone angle while for  $R_p = 3$ , only the density-based (tabulated) solver underestimates the angle of the spray cone as Fig. 9b suggests. What becomes apparent from the comparison between the high and low inlet-pressure data is that the discrepancies between numerical predictions and experiments do not exhibit any particular trend dependent on the superheat value. For instance, cases 6 and 9 share the same value of  $R_p = 7$ , yet the level of solver accuracy differs and hence the underlying

cause should be sought in delicate features inherent to flash boiling such as the degree of liquid metastability and the complementary influence of transient processes that cannot be captured in full [34], especially by the density-based solver where thermodynamic equilibrium is postulated.

Fig. 10 presents, in a comparative manner between the two solvers, the distribution of characteristic quantities along the axis of symmetry, for the two inlet-pressure values examined. The comparison reveals differences between the two methods, along with advantages and limitations. To distinguish between the presented curves, a solid line has been used for the 4-bar-inlet cases and a dotted line for the 8-bar-inlet. Varying superheat level results in different curves each marked with coloured points that, depending on the variable, may indicate the location of local minimum/maximum. To further elucidate distinct features of the flow expansion, four regions have been marked in Fig. 10. Marker “1”, points to the nozzle exit ( $X/D = 0$ ) region, with pressure being the variable of interest. The pressure-based solver (realising a mass-transfer based modelling approach) predicts a region immediately downstream of the exit of the nozzle where the pressure remains unchanged (Fig. 10a, left panel), suggesting the presence of a liquid core as also demonstrated by the constant density values in the region (Fig. 10c, left panel). On the contrary, the density-based (tabulated-thermodynamics) solver predicts an almost instant phase-change response of the fluid (Fig. 10c, right panel) to pressure change, also correlated to pressure fluctuations in the outlet region, refer to Marker “1” on the right-hand side panel of Fig. 10a. This behaviour is expected due to the infinite phase-change rate replicated through the use of the equation of

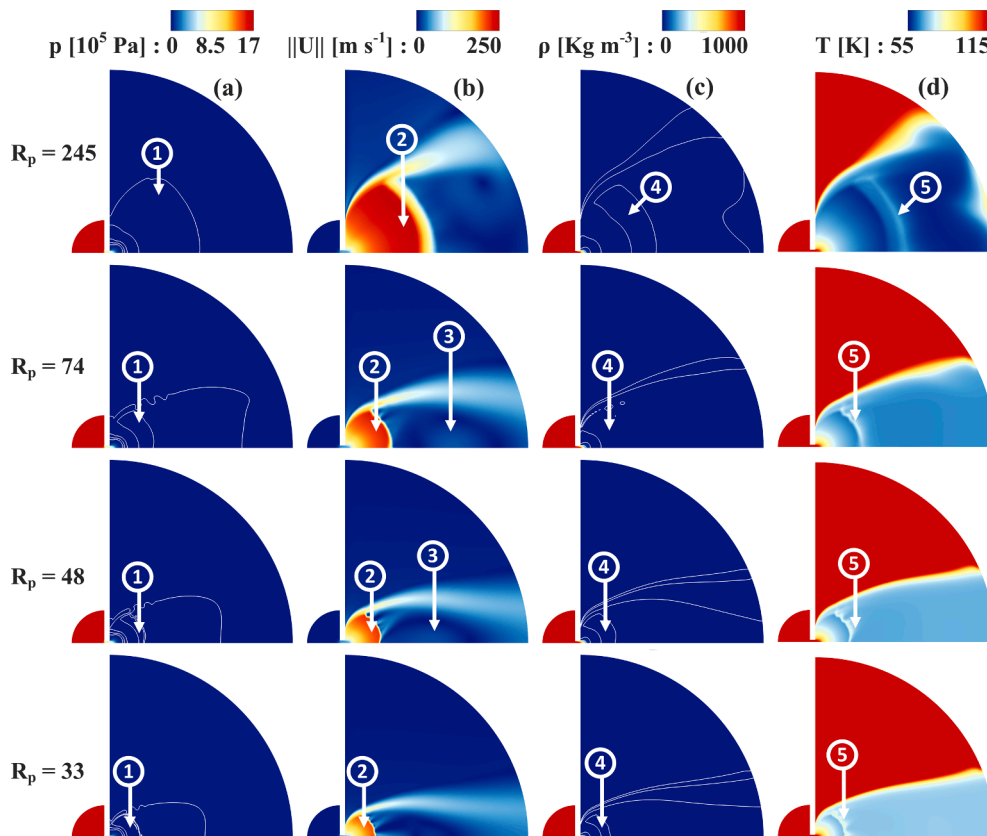


Fig. 8. Contour plots of (a) pressure, (b) axial velocity, (c) density and (d) temperature distribution for cases 1 to 4 of Table 2. Numbered markers annotate distinct features of the two-phase flow and temperature fields.

Table 3

Comparison between numerical predictions and experimental measurements for LN<sub>2</sub> mass flow rate in injector B.

Mass Flow Rate [kg m <sup>-3</sup> ]	Cases 5, 6, 7	Cases 8, 9, 10
Experimental	0.017 (±0.0005)	0.0097 (±0.0001)
Pressure-based	0.01859	0.01141
Density-based	0.01713	0.01058

state.

Regarding flow velocity presented in Fig. 10b, the pressure-based solver predicts a steeper increase, i.e., a more violent flow expansion, reaching a higher maximum velocity value (Marker “2”) compared to the density-based solver. This behaviour is attributed to the sonic velocity that, in essence, adjusts the flow velocity within the nozzle and is dependent on the phase-change rate, as it is designated by the two-phase mixture composition with lower sonic velocities obtained for bubbly mixtures. The density distribution along the axial coordinate at the nozzle symmetry axis (Fig. 10c) reveals that in the case of the pressure-based solver for different  $R_p$  values, phase change evolves in an identical, gradual manner, i.e., density distributions coincide (Marker “3”) until disrupted at the shockwave location. On the contrary, the density-based solver predictions on the right-hand side of the figure indicate an oscillating behaviour, potentially stemming from the averaging of a flapping pattern at the injector outlet since the density-based solver converges in a quasi-steady solution.

Finally, the temperature field is presented in Fig. 10d. As expected, temperature decreases sharply once phase change commences due to the conversion of sensible to latent heat required for the formation of bubbles. A subsequent temperature readjustment occurs in the pure-gas region. It must be noted that due to the ideal-gas assumption adopted

in the pressure-based solver, the minimum temperature in the domain had to be limited to the triple-point temperature (63.15 K), which, of course, constitutes a drawback of the thermodynamic-modelling approach. On the contrary, the density-based solver following a vapour-liquid equilibrium approach produces a physically accurate temperature field with the minimum temperature being approached asymptotically (Marker “4”).

Fig. 11 presents the radial velocity magnitude profiles of the expanding nitrogen flow as a function of the dimensionless cross-flow coordinate ( $Y/D$ ), calculated at a distance of two nozzle diameters ( $X/D = 2$ ) downstream the exit of the injection nozzle. The results for cases 6,7 and 9,10 of Table 2 follow a common trend indicating a flow acceleration pattern indicative of an under-expanded jet. Starting from the symmetry axis, velocity increases gradually up to the spray periphery where vapour fraction values are higher and thus compressibility effects are more pronounced.

The flow velocity subsequently decreases due to shearing with stagnant ambient. For the cases examined, this velocity decrease shows either a monotonical, Marker “1”, or a non-monotonical trend, Marker “2”. This behaviour is indicative of the morphology of the expansion cone, which, in turn, if the same  $R_p$  value is maintained, is designated by the inlet pressure, as illustrated in the inset of Fig. 11. Increased inlet pressure (8 bar) shifts the bell-shaped, flow-acceleration region downstream while it also increases its extent so as to overlap with the high-velocity region of the jet periphery. On the contrary, for an inlet pressure of 4 bar, the wake region past the shockwave (red arrow in the inset) intervenes between the expansion cone and the radial high-velocity zones producing the characteristic oscillating behaviour highlighted by Marker “2”.

The experimental investigation of Rees et al. [24] provides, apart from spray cone angles and mass flow rate measurements, shadowgraph images of the spray topology. To present a visual comparison between

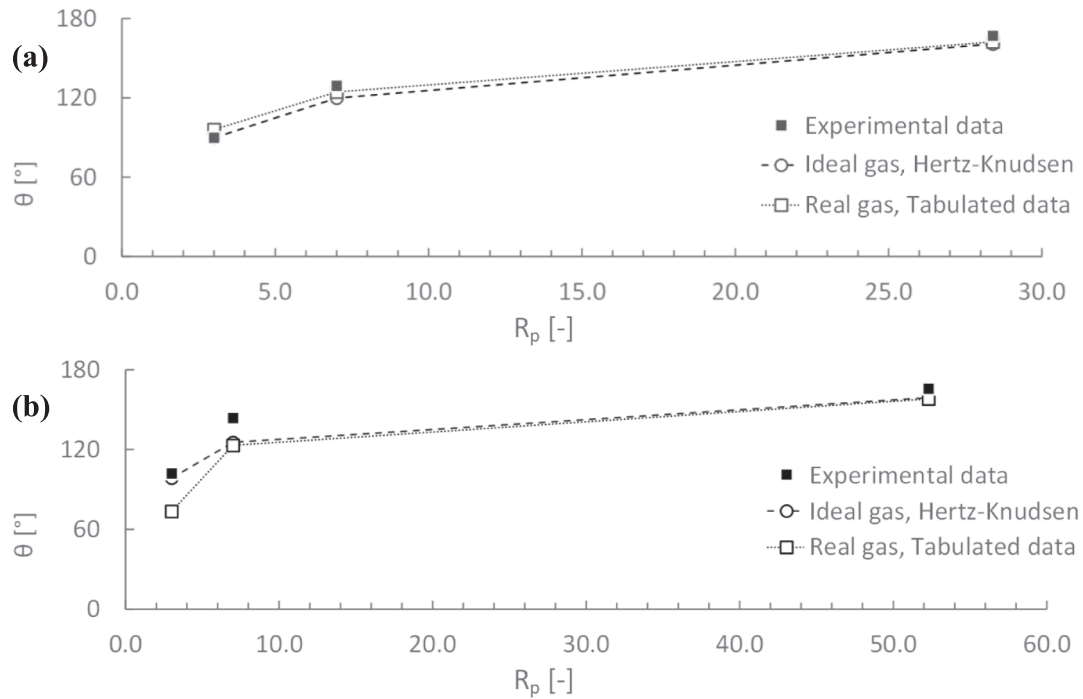


**Fig. 9.** Nitrogen spray cone angle for inlet pressure of (a) 8 bar corresponding to cases 5 to 7 of Table 2 and (b) 4 bar corresponding to cases 8 to 10 of Table 2 and comparison against the experimental values of [24]. Spray cone angles are measured at a distance equivalent to 2 nozzle diameters downstream of the nozzle exit.

the experimental images and numerical results, Fig. 12 has been compiled. For cases 8 to 10 of Table 2, experimental images are presented side-by-side with grayscale contours of the numerically-derived density gradient highlighting the locations of intense phase change. Although the numerical images constitute a slice of the spray, they do capture the spray topology resembling a bell-shaped hollow cone becoming more pronounced for increasing superheat, as demonstrated by the white (i.e., zero-gradient) regions around the axis of symmetry. The hemispherical region of steep gradients, which is abruptly terminated by the presence of the condensation shockwave is also reproduced accurately by the numerical results, as highlighted by the plots corresponding to the highest value of superheat. As can also be discerned, the spray cone becomes tangential to the nozzle outlet solid surface for high superheat values.

Complementary to Fig. 12, an illustration of the three-dimensional spray topology is presented in Fig. 13, resulting from a 180° revolution of a contour plot (produced for case 3) similar to those presented in Fig. 12. Since the experimental visualization technique is based on refractive index gradients, i.e., density changes, a density gradient iso-surface has been used to render the three-dimensional numerical spray representation. The slice contour plot on the right-hand side of Fig. 13 reveals distinct areas of steep density gradients, i.e., the expansion cone (region A), the shockwave location (region B) and the spray periphery (region C). By rotating this slice around the injector axis of symmetry, the topology shown on the left part of Fig. 13 is produced. As can be clearly seen, the resemblance with the qualitative experimental images of Fig. 12 is evident. The expansion-cone region directly downstream of the outlet appears darker due to the vigorous phase change and the presence of a pressure discontinuity, while a thin halo stemming from the periphery of the spray shrouds the regions further downstream leading to milder refractive index gradients.

#### 4. Conclusions

In this work, two-phase flashing flows of liquid oxygen and liquid nitrogen injected into near-vacuum conditions have been numerically investigated. For this purpose, a pressure- and a density-based solver

with two different approaches regarding the imposed phase-change rates and thermodynamics closure have been employed and their predictive capabilities have been evaluated. For the pressure-based solver, the departure from thermodynamic equilibrium during phase-change has been taken into account via the implementation of a bubble-dynamics model employing the Hertz-Knudsen equation, whereas thermodynamic equilibrium has been adopted in the density-based solver. Tabulated data for the variation of the fluid thermodynamic properties have been derived by the Helmholtz Equation of State (EoS) and used for the density solver operation. All the numerical results were compared against experimental data available in the literature.

The comparison demonstrated that both employed methodologies are suitable for calculating the evolution of a cryogenic flow expansion, phase-change/flashing and spray atomisation with certain advantages and limitations based on the inherent formulation of each technique. The Hertz-Knudsen phase-change model must be calibrated in order to model flash evaporation for various degrees of superheat. Therefore, in order to produce accurate results, initial calibration data must be available. The use of a thermodynamic table with real-gas thermodynamic properties produces accurate results for high superheat values while capturing the process with satisfactory accuracy for lower values of superheat. The level of accuracy differs among cases for reasons that can be sought in features inherent to flash boiling such as liquid metastability effects and the influence of transient processes that cannot be captured in full, especially by the density-based solver where thermodynamic equilibrium is postulated. The inherent inability of the method to account for metastability effects can be identified as a limitation of the presented methodology. Metastability effects could become important in transient flashing processes, as in blowdown tubes. Yet, for cryogenic fluid injection, which occurs under steady conditions, the method is sufficiently accurate and presents the advantage that, after the initial table of fluid properties is created for a range of conditions, no calibration is needed, unlike models based on a vapour-transport equation, since the phase change rate is dictated by the tabulated real-gas thermodynamics. Therefore, the tabulated approach can be utilized regardless the boundary conditions or the geometry.



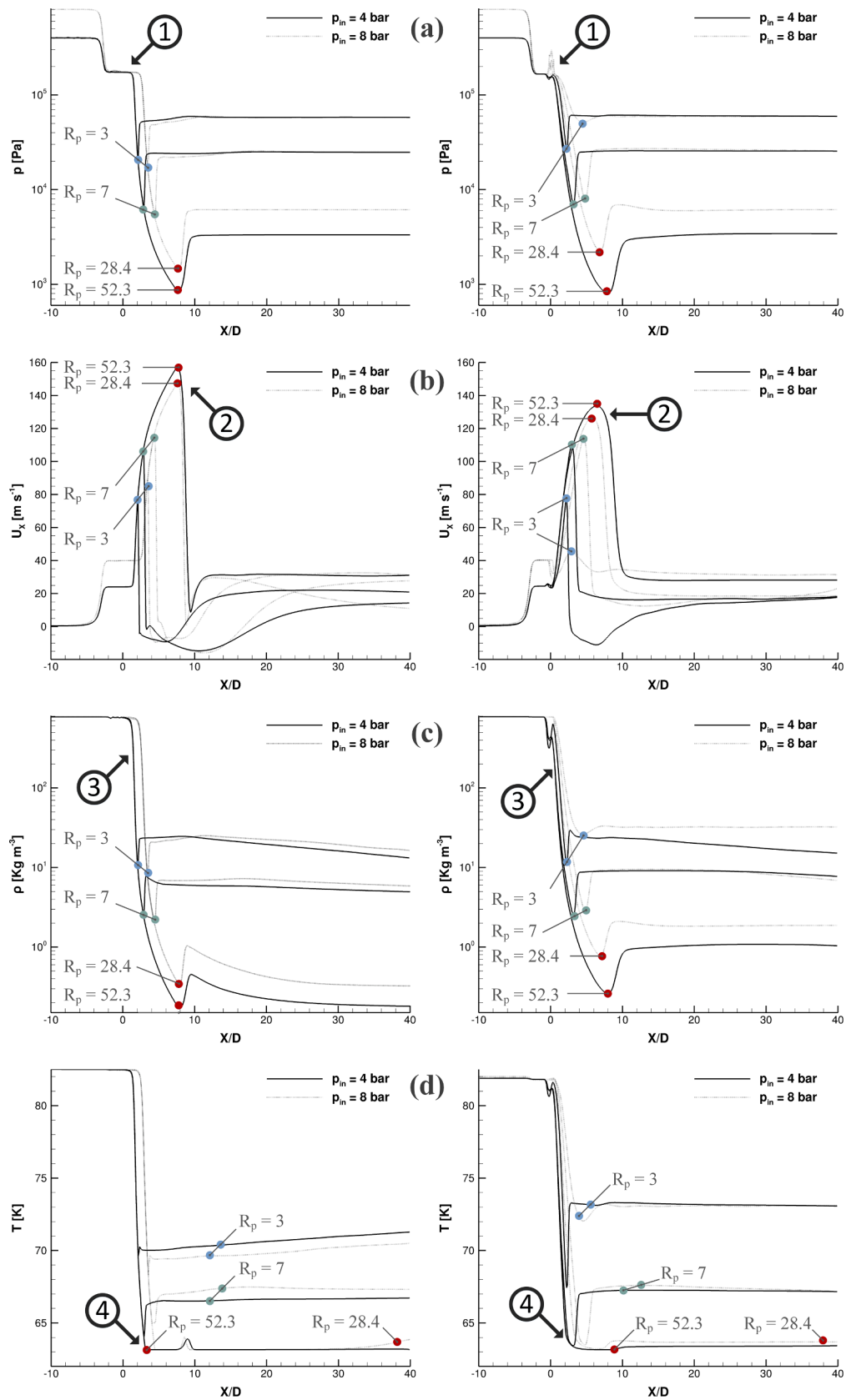


Fig. 10. Time-averaged values resulting from the use of pressure-based solver (left) and density-based solver (right). Distribution of (a) Pressure, (b) Axial Velocity, (c) Density and (d) Temperature along the nozzle axis of symmetry for cases 5 to 10 of Table 2.

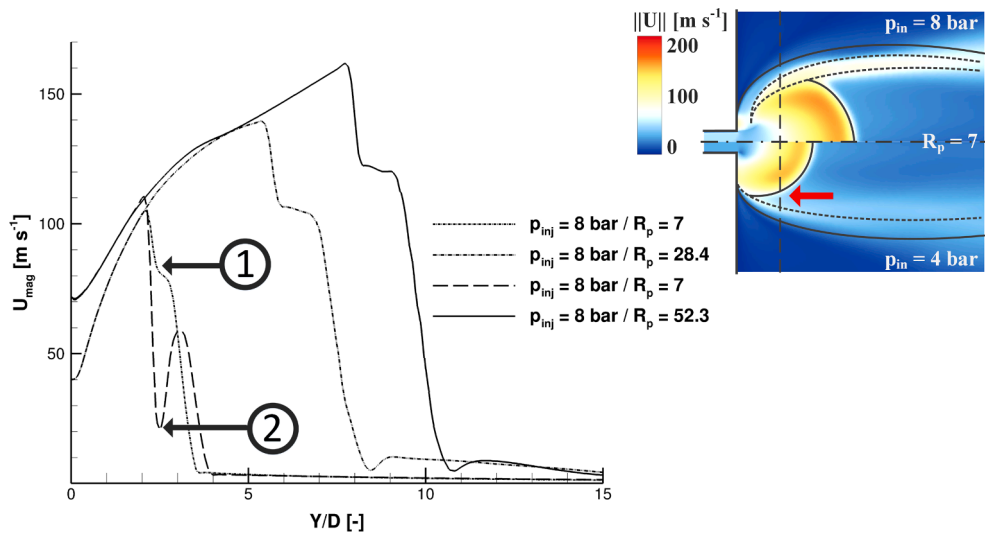


Fig. 11. (a) Velocity profiles for cases 6,7,9 and 10 of Table 2 at  $X/D = 2$  as a function of the dimensionless radial coordinate  $Y/D$ . Inset depicts velocity contour plots in the near-nozzle region of cases 6 (upper panel) and 9 (lower panel) of Table 2,  $R_p = 7$ .

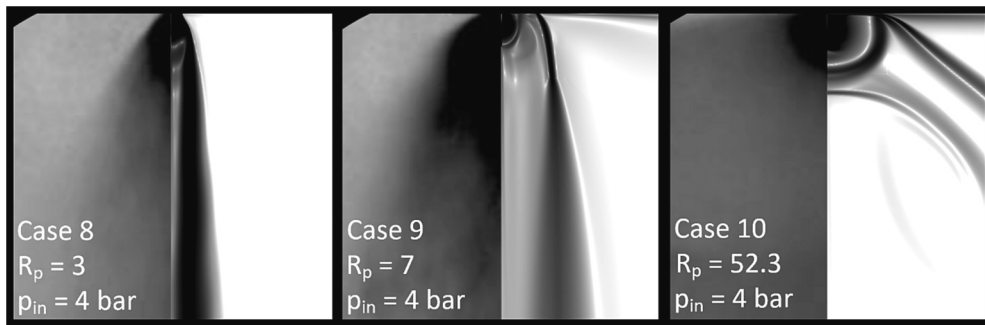


Fig. 12. Nitrogen injection, cases 8 to 10 of Table 2. Comparison between shadowgraphy images as presented by Rees et. al [24] (left panel of each frame) and numerically derived results using the density-based, tabulated solver (right panel). Density gradient magnitude has been plotted using a logarithmic scale with a darker colour corresponding to higher gradients similar to the colour band of Fig. 13.

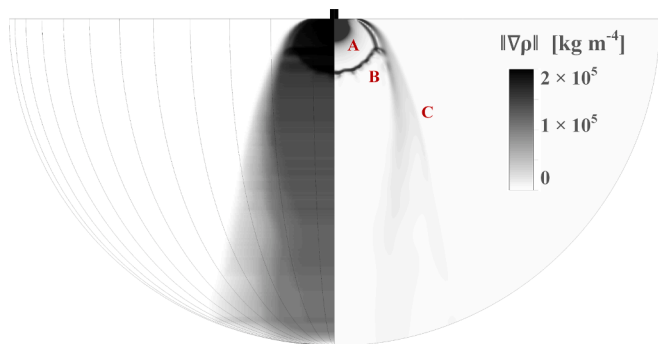


Fig. 13. Rendering of three-dimensional spray topology by revolution of the density gradient contour (left). Density gradient contour plot (right). Numerical data correspond to case 3,  $R_p = 74$  of Table 2.

**Declaration of Competing Interest**

The authors declare that they have no known competing financial interests or personal relationships that could have appeared to influence the work reported in this paper.

**Data availability**

Data will be made available on request.

**Acknowledgement**

The presented work has received funding from the European Union Horizon 2020 Research and Innovation programme as part of the ‘‘Holistic Approach of Spray Injection through a Generalized Multi-phase Framework (HAoS)’’ project. Grant Agreement ID: 675676.

**References**

- [1] K. Harstad, J. Bellan, Interactions of fluid oxygen drops in fluid hydrogen at rocket chamber pressures, *Int. J. Heat Mass Transf.* 41 (22) (1998) 3551–3558, [https://doi.org/10.1016/S0017-9310\(98\)00048-9](https://doi.org/10.1016/S0017-9310(98)00048-9).
- [2] D. Bradley, K. Van Hooser, Space Shuttle Main Engine - The Relentless Pursuit of Improvement, in: *AIAA SPACE, Conference & Exposition Long Beach, California: American Institute of Aeronautics and Astronautics*, Sep. 2011, 2011, <https://doi.org/10.2514/6.2011-7159>.
- [3] D. Davis and J. McArthur, NASA Ares I Crew Launch Vehicle Upper Stage Overview, in: *44th AIAA/ASME/SAE/ASEE Joint Propulsion Conference & Exhibit*, Hartford, CT: American Institute of Aeronautics and Astronautics, Jul. 2008. doi: 10.2514/6.2008-4897.
- [4] V. Yang, Liquid-Propellant Rocket Engine Injector Dynamics and Combustion Processes at Supercritical Conditions, in: *Defense Technical Information Center*, Fort Belvoir, VA, 2004, <https://doi.org/10.21236/ADA428947>.
- [5] D. Coulon, Vulcain-2 Cryogenic Engine Passes First Test with New Nozzle Extension, *ESA Bulletin* 102 (2000) 123–124.

- [6] L. Dreyer, Latest developments on SpaceX's Falcon 1 and Falcon 9 launch vehicles and Dragon spacecraft, in: IEEE Aerospace conference, IEEE, Big Sky, MT, USA, 2009, pp. 1–15, <https://doi.org/10.1109/AERO.2009.4839555>.
- [7] "Blue Origin Official Web-page." <https://www.blueorigin.com/engines/be-4>.
- [8] G.P. Sutton, History of Liquid Propellant Rocket Engines in the United States, *J. Propul. Power* 19 (6) (Nov. 2003) 978–1007, <https://doi.org/10.2514/2.6942>.
- [9] G.P. Sutton, History of Liquid-Propellant Rocket Engines in Russia, Formerly the Soviet Union, *J. Propul. Power* 19 (6) (Nov. 2003) 1008–1037, <https://doi.org/10.2514/2.6943>.
- [10] F.A. Boorady, D.A. Douglass, Solution of the high-vacuum hard-start problem of the IRFNA-UDMH rocket for Gemini Agena, *J. Spacecr. Rocket.* 5 (1) (Jan. 1968) 22–30, <https://doi.org/10.2514/3.29180>.
- [11] R. Schmehl, J. Steelant, Computational Analysis of the Oxidizer Pre-flow in an Upper-Stage Rocket Engine, *J. Propul. Power* 25 (3) (2009) 771–782, <https://doi.org/10.2514/1.38309>.
- [12] G. Lamanna, et al., Flashing Behavior of Rocket Engine Propellants, *Atom. Sprays* 25 (10) (2015) 837–856, <https://doi.org/10.1615/AtomizSpr.2015010398>.
- [13] M. Luo, O.J. Haidn, Characterization of Flashing Phenomena with Cryogenic Fluid Under Vacuum Conditions, *J. Propul. Power* 32 (5) (Sep. 2016) 1253–1263, <https://doi.org/10.2514/1.335963>.
- [14] R.C. Hendricks, R.J. Simoneau, and R.F. Barrows, Two-phase choked flow of subcooled oxygen and nitrogen, *STIN* 18376, 1976.
- [15] W. Mayer, H. Tamura, Propellant injection in a liquid oxygen/gaseous hydrogen rocket engine, *J. Propul. Power* 12 (6) (1996) 1137–1147, <https://doi.org/10.2514/3.24154>.
- [16] W.O.H. Mayer, et al., Atomization and Breakup of Cryogenic Propellants Under High-Pressure Subcritical and Supercritical Conditions, *J. Propul. Power* 14 (5) (Sep. 1998) 835–842, <https://doi.org/10.2514/2.5348>.
- [17] L. Vingert, G. Ordonneau, N. Ffida, and P. Grenard, A Rocket Engine under a Magnifying Glass, *AerospaceLab J.*, vol. Issue 11, p. 13 pages, 2016, doi: 10.12762/2016.AL11-15.
- [18] M. Habiballah, M. Orain, F. Grisch, L. Vingert, P. Gicquel, Experimental Studies of High-Pressure Cryogenic Flames on the Mascotte Facility, *Combust. Sci. Technol.* 178 (1–3) (2006) 101–128, <https://doi.org/10.1080/00102200500294486>.
- [19] B. Chehroudi, D. Talley, E. Coy, Visual characteristics and initial growth rates of round cryogenic jets at subcritical and supercritical pressures, *Phys. Fluids* 14 (2) (2002) 850–861, <https://doi.org/10.1063/1.1430735>.
- [20] B. Chehroudi, Recent Experimental Efforts on High-Pressure Supercritical Injection for Liquid Rockets and Their Implications, *Int. J. Aerosp. Eng.* 2012 (2012) 1–31, <https://doi.org/10.1155/2012/121802>.
- [21] G. Lamanna, Cryogenic Flashing Jets: A Review (Invited Paper), in: 52nd AIAA/SAE/AESE Joint Propulsion Conference, Salt Lake City, UT: American Institute of Aeronautics and Astronautics, Jul. 2016. doi: 10.2514/6.2016-4787.
- [22] G. Lamanna, H. Kamoun, B. Weigand, J. Steelant, Towards a unified treatment of fully flashing sprays, *Int. J. Multiph. Flow* 58 (2014) 168–184, <https://doi.org/10.1016/j.ijmultiphaseflow.2013.08.010>.
- [23] A. Rees, H. Salzmann, J. Sender, M. Oschwald, About the Morphology of Flash Boiling Liquid Nitrogen Sprays, *Atomiz. Spr.* 30 (10) (2020) 713–740, <https://doi.org/10.1615/AtomizSpr.2020035265>.
- [24] A. Rees, H. Salzmann, J. Sender, M. Oschwald, Investigation of Flashing LN<sub>2</sub>-Jets in Terms of Spray Morphology, Droplet Size and Velocity Distributions, p. 13 pages, 2019, doi: 10.13009/EUCASS2019-418.
- [25] W. Zhao, J. Yan, S. Gao, T.H. Lee, X. Li, Effects of fuel properties and aerodynamic breakup on spray under flash boiling conditions, *Appl. Therm. Eng.* 200 (2022), 117646, <https://doi.org/10.1016/j.applthermaleng.2021.117646>.
- [26] M.M. Khan, J. Hélie, M. Gorokhovskii, N.A. Sheikh, Experimental and numerical study of flash boiling in gasoline direct injection sprays, *Appl. Therm. Eng.* 123 (2017) 377–389, <https://doi.org/10.1016/j.applthermaleng.2017.05.102>.
- [27] C. Wang, Y. Song, P. Jiang, Modelling of liquid nitrogen spray cooling in an electronic equipment cabin under low pressure, *Appl. Therm. Eng.* 136 (2018) 319–326, <https://doi.org/10.1016/j.applthermaleng.2018.02.095>.
- [28] E. Sher, T. Bar-Kohany, A. Rashkovan, Flash-boiling atomization, *Prog. Energy Combust. Sci.* 34 (4) (2008) 417–439, <https://doi.org/10.1016/j.pecs.2007.05.001>.
- [29] X. Zhu, et al., Thermal nonequilibrium and mechanical forces induced breakup and droplet formation of superheated liquid jets under depressurized release, *Appl. Therm. Eng.* 221 (2023), 119826, <https://doi.org/10.1016/j.applthermaleng.2022.119826>.
- [30] M.S. Khan, I.A. Karimi, D.A. Wood, Retrospective and future perspective of natural gas liquefaction and optimization technologies contributing to efficient LNG supply: A review, *J. Nat. Gas Sci. Eng.* 45 (Sep. 2017) 165–188, <https://doi.org/10.1016/j.jngse.2017.04.035>.
- [31] L. Wang, X. Ma, H. Kong, R. Jin, H. Zheng, Investigation of a low-pressure flash evaporation desalination system powered by ocean thermal energy, *Appl. Therm. Eng.* 212 (Jul. 2022), 118523, <https://doi.org/10.1016/j.applthermaleng.2022.118523>.
- [32] P. Srivastava, A. Kumar, Characterization of performance of multihole nozzle in cryospray, *Cryobiology* 96 (Oct. 2020) 197–206, <https://doi.org/10.1016/j.cryobiol.2020.06.008>.
- [33] M. Foerster, T. Gengenbach, M.W. Woo, C. Selomulya, The impact of atomization on the surface composition of spray-dried milk droplets, *Colloids Surf. BBiointerfaces* 140 (Apr. 2016) 460–471, <https://doi.org/10.1016/j.colsurfb.2016.01.012>.
- [34] Y. Liao, D. Lucas, A review on numerical modelling of flashing flow with application to nuclear safety analysis, *Appl. Therm. Eng.* 182 (Jan. 2021), 116002, <https://doi.org/10.1016/j.applthermaleng.2020.116002>.
- [35] Y. Liao, D. Lucas, Computational modelling of flash boiling flows: A literature survey, *Int. J. Heat Mass Transf.* 111 (Aug. 2017) 246–265, <https://doi.org/10.1016/j.ijheatmasstransfer.2017.03.121>.
- [36] J. R. Travis, D. Piccioni Koch, W. Breitung, A homogeneous non-equilibrium two-phase critical flow model, *Int. J. Hydrogen Energy*, vol. 37, no. 22, pp. 17373–17379, 2012, doi: 10.1016/j.ijhydene.2012.07.077.
- [37] K. Lyras, S. Dembele, D.P. Schmidt, J.X. Wen, Numerical simulation of subcooled and superheated jets under thermodynamic non-equilibrium, *Int. J. Multiph. Flow* 102 (2018) 16–28, <https://doi.org/10.1016/j.ijmultiphaseflow.2018.01.014>.
- [38] J. Chen, X. Gao, S. Bao, L. Hu, J. Xie, Numerical analysis of spray characteristics with liquid nitrogen, *Cryogenics* 109 (Jul. 2020), 103113, <https://doi.org/10.1016/j.cryogenics.2020.103113>.
- [39] J.W. Gärtner, A. Kronenburg, A. Rees, J. Sender, M. Oschwald, G. Lamanna, Numerical and experimental analysis of flashing cryogenic nitrogen, *Int. J. Multiph. Flow* 130 (Sep. 2020), 103360, <https://doi.org/10.1016/j.ijmultiphaseflow.2020.103360>.
- [40] D.D. Loureiro, J. Reutzsch, A. Kronenburg, B. Weigand, K. Vogiatzaki, Primary breakup regimes for cryogenic flash atomization, *Int. J. Multiph. Flow* 132 (Nov. 2020), 103405, <https://doi.org/10.1016/j.ijmultiphaseflow.2020.103405>.
- [41] D.D. Loureiro, A. Kronenburg, J. Reutzsch, B. Weigand, K. Vogiatzaki, Droplet size distributions in cryogenic flash atomization, *Int. J. Multiph. Flow* 142 (Sep. 2021), 103705, <https://doi.org/10.1016/j.ijmultiphaseflow.2021.103705>.
- [42] T. Ramcke, A. Lampmann, M. Pfitzner, Simulations of Injection of Liquid Oxygen/Gaseous Methane Under Flashing Conditions, *J. Propul. Power* 34 (2) (2018) 395–407, <https://doi.org/10.2514/1.336412>.
- [43] P. Koukouvini, A. Vidal-Roncero, C. Rodriguez, M. Gavaises, L. Pickett, High pressure/high temperature multiphase simulations of dodecane injection to nitrogen: Application on ECN Spray-A, *Fuel* 275 (2020), 117871, <https://doi.org/10.1016/j.fuel.2020.117871>.
- [44] A. Vidal, K. Kolovos, M.R. Gold, R.J. Pearson, P. Koukouvini, M. Gavaises, Preferential cavitation and friction-induced heating of multi-component Diesel fuel surrogates up to 450MPa, *Int. J. Heat Mass Transf.* 166 (2021), 120744, <https://doi.org/10.1016/j.ijheatmasstransfer.2020.120744>.
- [45] T. Lyras, I.K. Karathanassis, N. Kyriazis, P. Koukouvini, M. Gavaises, Modelling of liquid oxygen nozzle flows under subcritical and supercritical pressure conditions, *Int. J. Heat Mass Transf.* 177 (2021), 121559, <https://doi.org/10.1016/j.ijheatmasstransfer.2021.121559>.
- [46] I.K. Karathanassis, P. Koukouvini, M. Gavaises, Comparative evaluation of phase-change mechanisms for the prediction of flashing flows, *Int. J. Multiph. Flow* 95 (2017) 257–270, <https://doi.org/10.1016/j.ijmultiphaseflow.2017.06.006>.
- [47] N. Kyriazis, P. Koukouvini, M. Gavaises, Numerical investigation of bubble dynamics using tabulated data, *Int. J. Multiph. Flow* 93 (2017) 158–177, <https://doi.org/10.1016/j.ijmultiphaseflow.2017.04.004>.
- [48] N. Kyriazis, P. Koukouvini, I. Karathanassis, M. Gavaises, A Tabulated Data Technique For Cryogenic Two-Phase Flows. 6th European Conference on Computational Mechanics (ECCM 6), 7th European Conference on Computational Fluid Dynamics (ECFD 7), Glasgow UK, 2018.
- [49] S. Schmidt, I. Sezal, G. Schnerr, and M. Talhamer, Riemann Techniques for the Simulation of Compressible Liquid Flows with Phase-Transition at all Mach Numbers - Shock and Wave Dynamics in Cavitating 3-D Micro and Macro Systems, in: 46th AIAA Aerospace Sciences Meeting and Exhibit, Reno, Nevada: American Institute of Aeronautics and Astronautics, 2008. doi: 10.2514/6.2008-1238.
- [50] M.-S. Liou, A sequel to AUSM, Part II: AUSM+–up for all speeds, *J. Comput. Phys.* 214 (1) (2006) 137–170, <https://doi.org/10.1016/j.jcp.2005.09.020>.
- [51] E.F. Toro, *Riemann Solvers and Numerical Methods for Fluid Dynamics: A Practical Introduction*. Springer Berlin Heidelberg, 2013. [Online]. Available: <https://books.google.gr/books?id=zKLiCAAQBAJ>.
- [52] D. Fuster, G. Hauke, C. Dopazo, Influence of the accommodation coefficient on nonlinear bubble oscillations, *J. Acoust. Soc. Am.* 128 (1) (2010) 5–10, <https://doi.org/10.1121/1.3436520>.
- [53] C.E. Brennen, *Cavitation and bubble dynamics*, Cambridge University Press, New York, 2014.
- [54] B.M. Devassy, D. Benković, Z. Petranovic, W. Edelbauer, M. Vujanovic, *Numerical Simulation of Internal Flashing in a GDI Injector Nozzle*. 29th Conference on Liquid Atomization and Spray Systems, Paris, France, 2019.
- [55] E.W. Lemmon, R. Tillner-Roth, A Helmholtz energy equation of state for calculating the thermodynamic properties of fluid mixtures, *Fluid Phase Equilib.* 165 (1) (1999) 1–21, [https://doi.org/10.1016/S0378-3812\(99\)00262-9](https://doi.org/10.1016/S0378-3812(99)00262-9).
- [56] M. Dumbser, U. Ben, C.-D. Munz, Efficient implementation of high order unstructured WENO schemes for cavitating flows, *Comput. Fluids* 86 (2013) 141–168, <https://doi.org/10.1016/j.compfluid.2013.07.011>.
- [57] F.R. Menter, Two-equation eddy-viscosity turbulence models for engineering applications, *AIAA J.* 32 (8) (1994) 1598–1605, <https://doi.org/10.2514/3.12149>.
- [58] N. Kyriazis, P. Koukouvini, M. Gavaises, Modelling cavitation during drop impact on solid surfaces, *Adv. Colloid Interface Sci.* 260 (2018) 46–64, <https://doi.org/10.1016/j.cis.2018.08.004>.